Geophysical Journal International

Geophys. J. Int. (2019) **216,** 1665–1674
Advance Access publication 2018 December 06
GJI Geodynamics and tectonics

doi: 10.1093/gji/ggy514

Interaction of the Cyprus/Tethys slab with the mantle transition zone beneath Anatolia

George Taylor [1,*] David A. Thompson [2,†] David Cornwell [3] and Sebastian Rost [1]

[1] *School of Earth and Environment, University of Leeds, Woodhouse Lane, LS2 9JT, UK. E-mail: s.rost@leeds.ac.uk*
[2] *School of Earth and Ocean Sciences, Cardiff University, Park Place, CF10 3AT, UK*
[3] *School of Geosciences, University of Aberdeen, King's College, AB24 3UE, UK*

Accepted 2018 December 4. Received 2018 November 15; in original form 2018 June 28

SUMMARY

The interaction of subducted oceanic lithosphere with the discontinuities of the mantle transition zone (MTZ) provides insight into the composition and temperature of the subducted slab as well as potential melting of the slab or the surrounding mantle and loss of volatiles from the slab. Detailed mapping of the structure of the MTZ will help to better understand how slabs transport material and volatiles into the mantle and how phase transitions affect the slab dynamics. Here we use a dense network of seismic stations in northern Anatolia to image the structure of the MTZ discontinuities in detail using *P*-wave receiver functions. With a station spacing of about 7 km and a surface footprint of ∼35 km × ∼70 km, analysing receiver functions calculated from teleseismic earthquakes that occurred during an ∼18-month deployment produced clear images of where the MTZ interacts with the Tethys/Cyprus slabs that either lie flat on the 660-km discontinuity or pass into the lower mantle. We observe an undulating 660-km discontinuity depressed by up to 30 km and a slightly depressed (1–2 km) 410-km discontinuity, apparently undisturbed by the slab. The MTZ is thickened to ∼270 km as result of the cool slab in the MTZ influencing the 660-km discontinuity and includes an arrival at ∼520-km depth likely from the top of a flat lying slab or a discontinuity related to a solid–solid phase transition in the olivine component of the mantle. We find evidence for low-velocity zones both above and below the 410-km discontinuity and above the 660-km discontinuity. The low-velocity zones around the 410-km discontinuity might be the result of hydration of the MTZ from the slab and upward convection of MTZ material into the upper mantle. The origin of the low-velocity zone around the 660-km discontinuity is less clear and could be related to sedimentation of subducted mid-ocean ridge basalts. The small footprint of the seismic array provides accurate information on the structure of the MTZ in an area influenced by subduction and shows small-scale changes in MTZ structure that might be lost in studies covering larger areas with sparser sampling.

Key words: Composition and structure of the mantle; Phase transitions; Mantle processes; Dynamics of lithosphere and mantle; Subduction zone processes.

INTRODUCTION

Subducted slabs are a major pathway for oceanic lithosphere, continental sediments and volatiles to be transported into the lower mantle. Constraining this process and the interaction of the slab with the mantle at different depths are essential for our understanding of the flux and storage of elements such as carbon and water into the lower mantle and has an impact on life and the long-term habitability of Earth (Dasgupta & Hirschmann 2010; Schmandt *et al.* 2014). The upper mantle beneath the eastern Mediterranean has long been influenced by interactions with subducted material due to the closure of the Tethys ocean and the ongoing subduction at the Hellenic and Cyprus trenches (Robertson & Dixon 1984; Stampfli 2000; Cavazza *et al.* 2004; Faccenna *et al.* 2006; Jolivet *et al.* 2013). It is therefore an ideal location to study the interaction of subducted material with the upper mantle.

* Now at Institute of Seismology, School of Geosciences and Geography, University of Helsinki, Helsinki 00014, Finland.
† Formerly at School of Geosciences, University of Aberdeen, King's College, AB24 3UE, UK and School of Earth and Environment, University of Leeds, Woodhouse Lane, LS2 9JT, UK.

The mantle transition zone (MTZ) is bounded by two global seismic discontinuities located at depths of approximately 410 and 660 km. These sharp increases in seismic velocity are typically attributed to solid–solid phase transitions in the olivine component of the mantle. The 410-km discontinuity (herewith 'the 410') marks the transition from α-olivine to wadsleyite, while the 660-km discontinuity (herewith 'the 660') is due to a transition from ringwoodite to bridgmanite and magnesiowüstite (Frost 2008). The depths of the 410 and 660 transitions are dependent on pressure and temperature (e.g. Helffrich 2000), allowing MTZ thickness to be used to infer the thermal state of the mantle (Shearer & Masters 1992; Flanagan & Shearer 1998; Schmerr & Garnero 2006). The 410 transition occurs at lower pressures (and hence at shallower depths) in the presence of lower temperatures, while the opposite Clapeyron slope of the 660 means it will occur deeper in regions of lower temperature (e.g. Helffrich 2000). Increased temperatures will conversely result in a deeper 410, and a shallower 660, resulting in a thinned MTZ. Theoretical and experimental studies on the petrology of upper-mantle material have also shown that the composition and water content of the mantle strongly influence the structure and depth of these discontinuities (Bolfan-Casanova *et al.* 2006).

An additional discontinuity at a depth of about 520 km (the 520) has also been observed at several locations (Shearer 1990) and might be related to the wadsleyite–ringwoodite phase transition (Sinogeikin 2003) or the formation of $CaSiO_3$ bridgmanite from garnet (Saikia *et al.* 2008). The 520 has been found to occur over a diffuse depth range and therefore might not be sharp enough to observe seismically and observations remain controversial (Bock 1994). The 520 might be observable in subduction zones (Gilbert *et al.* 2001) where the wadsleyite–ringwoodite phase transition may occur over a small pressure interval due to variations in olivine content (Gu *et al.* 1998), hydrated mantle or slab material (Inoue *et al.* 1998).

Mineral–physical studies have shown that water content influences the properties of the olivine–wadsleyite phase transition (Smyth & Frost 2002; Ohtani 2005). Water is preferentially incorporated into wadsleyite rather than olivine, so the transition zone has a larger water storage capability than the upper or lower mantle. This could lead to dehydration melting in material moving upwards through the 410, or sinking through the 660 (Revenaugh & Sipkin 1994; Bercovici & Karato 2003; Schmandt *et al.* 2014). It is possible that the related partial melting could be observed as zones of low seismic velocity bounding the transition zone discontinuities (Revenaugh & Sipkin 1994).

The eastern Mediterranean has a long and complex tectonic history currently characterized by differential plate motions between Arabia/Eurasia and by active subduction at the Hellenic and Cyprus trenches (Pichon & Angelier 1979; Pichon *et al.* 1981). It has been proposed that the material being subducted at these trenches is some of the oldest oceanic lithosphere on the planet and might be a remnant of the closure of the Neo- and Palaeo-Tethys oceans (Hafkenscheid *et al.* 2006; Granot 2016).

Tomographic images of the upper mantle in the region show the location of the subducted material from the active trenches to the top of the lower mantle (Bijwaard *et al.* 1998; Goes *et al.* 1999; Piromallo & Morelli 2003; Berk Biryol *et al.* 2011; Salaün *et al.* 2012; Fichtner *et al.* 2013a,b; Paul *et al.* 2014; Zhu *et al.* 2015), with evidence for a long lasting tear in the slab at the Isparta angle influencing the dynamics of the region (Bijwaard *et al.* 1998; Jolivet *et al.* 2009, 2013; Berk Biryol *et al.* 2011). Although the tomographic images show that the flow of the eastern Mediterranean slabs into the lower mantle could be impeded by the 660 beneath Anatolia (Berk Biryol *et al.* 2011), the Tethys slab has been detected in the lower mantle beneath India (Van der Voo *et al.* 1999; van der Meer *et al.* 2009). It therefore remains unclear exactly how the slabs interact with MTZ discontinuities beneath Anatolia and the location where it penetrates into the lower mantle.

This study utilises *P*-wave receiver functions (PRF; e.g. Langston 1979; Ammon 1991) from a dense network of seismometers deployed in northwestern Turkey to image the MTZ discontinuities beneath Anatolia (DANA 2012). Our results show that the MTZ is thickened to ∼270 km and contains a strong 520-km discontinuity, with evidence for multiple low-velocity layers around the discontinuities. This provides conclusive evidence for the presence of the slab and indicates a complex interplay of processes as the slab interacts with the MTZ beneath Anatolia.

DATA AND ANALYSIS

A temporary network (Fig. 1a) of 73 medium- and broad-band seismometers was deployed between May 2012 and October 2013 across the north Anatolian fault zone in the rupture zone of the 1999 Izmit earthquake (DANA 2012). The stations were deployed on a semi-regular rectangular grid of 6 lines east–west and 11 rows north–south. The nominal station spacing of the regular grid is 7 km. In addition to the main grid, a further seven stations were deployed in a half circle towards the east, with a larger station spacing.

We use instrument-response deconvolved *P*-waveforms from 160 high-quality teleseismic events (Fig. 1b) to compute PRF, isolating *P*-to-*S* wave conversions from seismic discontinuities beneath the array. The waveform data were initially filtered using a second-order Butterworth bandpass filter between 0.04 and 3.0 Hz. We used an iterative time domain deconvolution method (Ligorría & Ammon 1999) with a Gaussian pulse width of 0.625 to deconvolve the vertical component *P* waveform from both the radial and transverse components to isolate *P*-to-*S* wave conversions from the MTZ discontinuities. This approach leads to a dominant receiver function frequency of ∼0.3 Hz, which is the ultimate limit on the spatial resolution of this study. While the nature of our array (station spacing of ∼7 km) provides us with dense sampling within the MTZ (Fig. 1b), our horizontal resolution is limited by the size of the Fresnel zone radii within the MTZ (approximately 60–80 km). Visual inspection led to 2346 high-quality receiver functions sampling an area of ∼3° × 3° where slabs from the Mediterranean subduction zones (Hellenic and Cyprus slabs) have been imaged within the MTZ (Berk Biryol *et al.* 2011; Fig. 1b). This data set was further trimmed to 1505 of the highest quality PRFs following an automated signal-to-noise ratio procedure (Hetényi *et al.* 2009; Cornwell *et al.* 2011). The final data set of PRFs is dominated by ray paths that sample the MTZ to the north and east of the array (Fig. 1b). This ray geometry provides sampling in the region where the Hellenic and Cyprus slabs interact with the 660, while not sampling the transition of the slab through the 410 to the south of the region sampled by our data set. Figures for the full data set are shown in the Supporting Information with images produced with the quality selected data set shown in the main part of the manuscript.

PRFs were then migrated using three different approaches to first characterize the broad features and then examine their variation in space and depth. The first method is a 1-D time migration (Stoffa *et al.* 1981; Fig. 2) without corrections for crust- and upper-mantle velocity variations (Thompson *et al.* 2011) assuming the 1-D Earth model ak135 (Kennett *et al.* 1995). We then perform a 2-D common conversion point (CCP) migration (Sheehan *et al.* 2000) in depth

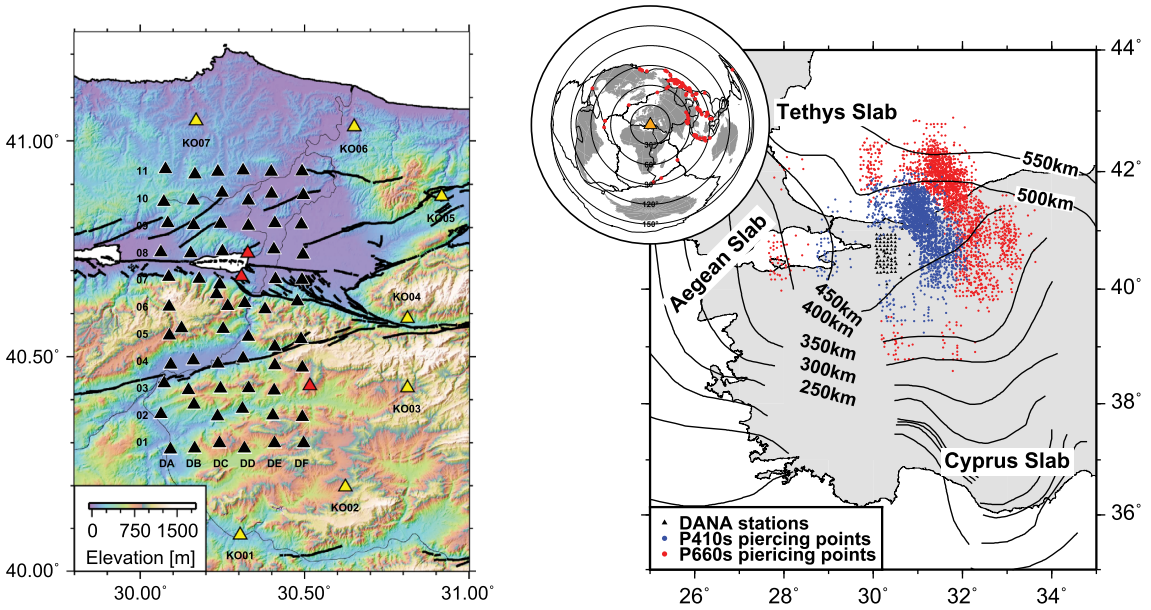

Figure 1. (a) DANA station locations. Stations of the regular grid are shown as black triangles and include three permanent stations of the KOERI national seismic network (red triangles). Yellow triangles indicate the eastern girdle of stations with larger station spacing. Background shows elevations from the Shuttle Radar Topography mission (Farr *et al.* 2007). (b) Receiver function piercing points at 410-km (blue) and 660-km depth (red). Station locations are indicated by small triangles. Slab depths from tomographic models are indicated by black lines and are from Berk Biryol *et al.* (2011).

again using the ak135 velocity model (Fig. 3). This migration collapses all the data from our small conversion point footprint into a 2-D N–S profile, with a minimum of 10 conversion points in an individual bin. Finally, we perform a 3-D CCP migration (Fig. 4) through the EU60 velocity model of Zhu *et al.* (2015) by binning into 15 km × 15 km × 2 km voxels and then accounting for the Fresnel zone size by applying a Gaussian smoothing operator over 5 (i.e. 75 km) neighbouring bins in the horizontal directions and 3 (i.e. 6 km) in the vertical direction (e.g. Hetényi *et al.* 2009).

RESULTS

The PRF results clearly show *P*-to-*S* conversions from the upper-mantle discontinuities. Fig. 2(a) shows stacked PRFs as a function of slowness. An *N*th-root ($N = 4$) slant stack for a reference slowness of 5.59 s deg^{-1} showing the observed seismic arrivals is also included in Fig. 2(b). The *P*-to-*S* conversions from the 410 and 660 are clearly visible arriving at ∼45 and ∼65 s, slightly later (∼2–3 s) than predicted by ak135. This could be due to the low *S*-wave velocities in the upper mantle beneath Anatolia (Salaün *et al.* 2012; Fichtner *et al.* 2013a; Zhu *et al.* 2015), but our data set cannot rule out the possibility that both the 410 and 660 are located slightly deeper than average in this location. Notably, the traveltime anomalies are consistent between the 410 and 660 arrival times, which suggest that the majority of this traveltime residual can be accounted for through velocity variations in the upper mantle above the 410 along the *S*-leg of the *P*-to-*S* conversion. Another positive arrival is located at times between 50 and 60 s, between the 410 and 660. The arrival time of this arrival varies as a function of slowness, arriving earlier at low slowness, and later at slownesses of greater than 6.5 s deg^{-1}. This arrival is most likely a *P*-to-*S* conversion from a discontinuity at approximately the 520, potentially related to the wadsleyite to ringwoodite transition. We also observe a lower amplitude positive arrival at 75–85 s, which corresponds to a lower mantle depth of ∼800 km (Figs 2 and 4). In addition to these positive arrivals, there are several negative arrivals present in the PRFs that suggest velocity decreases with depth (i.e. a low-velocity layer). These negative arrivals are particularly prominent at ∼40 and ∼50 s, bounding the 410. A further localized negative arrival can be seen above the 660 at ∼65 s, most evident at a slowness of larger than +6.5 s deg^{-1}. The moveout characteristics of these arrivals indicate that they are not multiples from shallower discontinuities (Fig. 2b).

The results of the 2-D and 3-D CCP depth migrations are shown in Figs 3 and 4, overlain onto the EU60 tomography model (Zhu *et al.* 2015). Vertical and horizontal resolution of these migrated receiver function images are estimated to be ±5 and 30 km, respectively, based on the first Fresnel zone at the relevant frequency. The 410 shows little depth variation along the 2-D radial PRF profile whereas the 660 shows minor undulations on the order of 10 km (Fig. 3). The maximum thickness of the transition zone in this transect is ∼270 km: thicker than the global average of 242 km (Gu & Dziewonski 2002). This thickening is the result of topography and an overall deepening of the 660, which is largest close to the subducted slab indicated by high seismic velocities in the tomographic model. A conversion from the 520 is visible in the centre of the profile (Fig. 3), close to the velocity gradient interpreted as the top of the slab in the EU60 tomography model (Zhu *et al.* 2015).

The 3-D CCP depth migration using the EU60 tomography model (Fig. 4) generally displays similar structures to those observed in the 2-D migrated profile (Fig. 3). Migration through the 3-D tomography model appears to remove part of the traveltime anomaly visible in the 1-D/2-D migrations, giving further support to an upper-mantle source of this traveltime anomaly. Some slight delay remains in the 3-D migrated images, indicating that the tomography model may underpredict the magnitude of the upper-mantle velocity anomalies in the region. The 410 is enclosed by negative arrivals, which can also be seen above the 660. A positive arrival from the 520 occurs at various locations, with a depth variation of ±20 km. This arrival is strongest in the centre of the profiles coinciding with the top of the high-velocity anomaly in the tomographic models. Negative arrivals

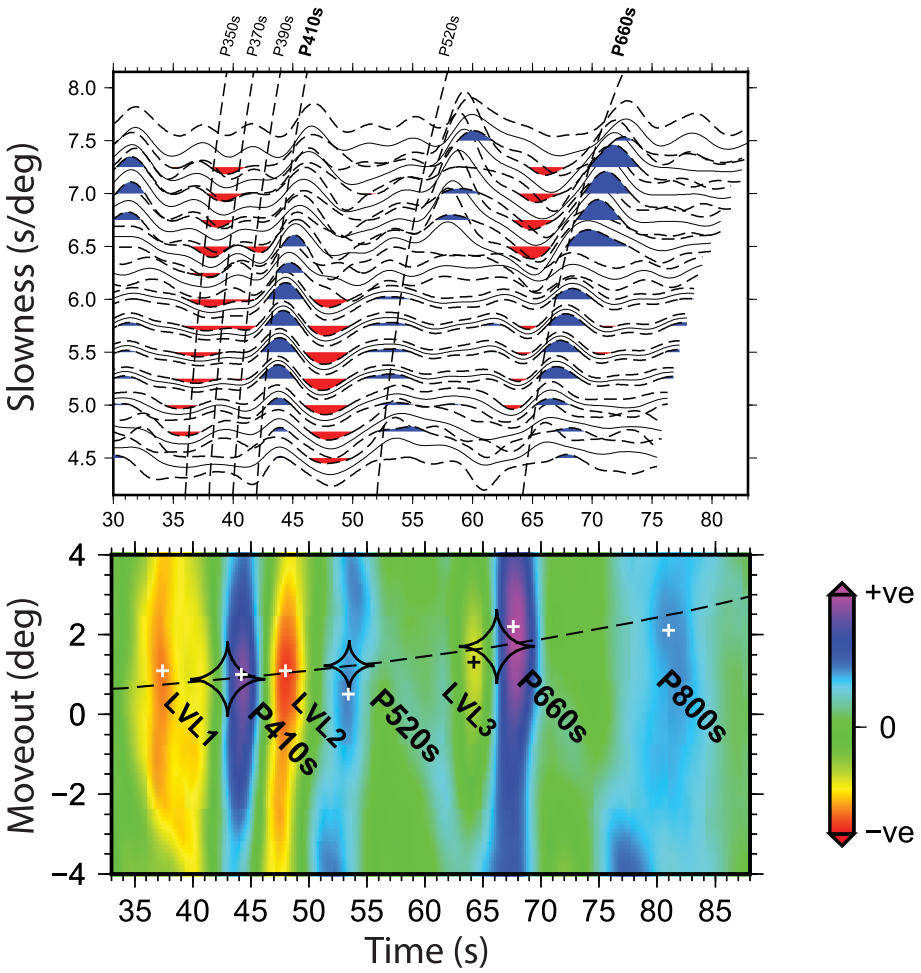

Figure 2. (a) Slowness section for the DANA network using the full data set, highlighting the arrivals from the 410-km (the 410) and 660-km discontinuities (the 660) and waveform variations from velocity variations. Predicted traveltimes for conversions from varying depths (dashed lines) have been calculated through the 1-D Earth model ak135 (Kennett *et al.* 1995). Also visible are conversions from an apparent depth of 520 km in some regions of the study area. Dashed lines are 2σ confidence limits. (b) Slant stack of receiver functions with a reference slowness of 5.59 s deg^{-1}. We observe strong arrivals from the 410 and 660 with strong low-velocity zones around the 410 and a weaker conversion from 520-km depth. A diffuse arrival from depths of about 800 km can also be observed. The 410 arrival shows strong negative arrivals from shallower and larger depths. Similarly, a lateral varying negative arrival can be observed for the 660.

around the 410 and 660 show clear lateral variations. The negative arrival above the 660 seems to be absent from the southern part of the profile, while the arrival from below the 410 is present almost everywhere. The arrival above the 410 appears more complex but is clearly visible in both the south and north of the profile.

Transverse PRFs were calculated using the deconvolution of the vertical from tangential components (see Supporting Information) to examine evidence for radial seismic anisotropy or *P*-to-*S* conversions from dipping structures. Although some energy is present, the data distribution might prevent any conclusive interpretation of this energy and there seems to be little consistent structure throughout the volume in these transverse PRFs. We therefore conclude that there are no major and robust radially anisotropic signals present in the MTZ in this region.

DISCUSSION

Our PRF results provide high-resolution images of the MTZ in the vicinity of a subducted slab. The tomographic models (shown in the background of Figs 2–4) indicate that a slab (defined by the high-velocity anomaly) is lying flat on the 660, although there is an alternative evidence that it penetrates the lower mantle (Bijwaard *et al.* 1998; Zhu *et al.* 2015; van der Meer *et al.* 2018). Our densely sampled receiver function images allow new detailed insight into the physical processes occurring during the interaction of the slab with the MTZ (Fig. 5).

In general, the main features of the data set are consistent between all migration approaches (Figs 2–4), though some lateral variations in the MTZ structure are apparent in the 3-D data set. The amplitude of the 410 conversion is quite variable in the 3-D migration, and is not clearly visible in the far west and east of the image (Fig. 4). In addition, the low-velocity zone below the 410, which is prevalent throughout the 1-D and 2-D migrations, is notable only in the northern parts of the 3-D migration (Fig. 4). Only the most eastern 3-D migration profile shows evidence of a low-velocity zone beneath the 410 in the south. Conversely, the 660 and its associated low-velocity zones are spatially consistent between both the 2-D and 3-D migrations. The comparison between the two sets of migrated images allows us to identify the more robust features of our data set (e.g. the location of the 660), alongside those features that show

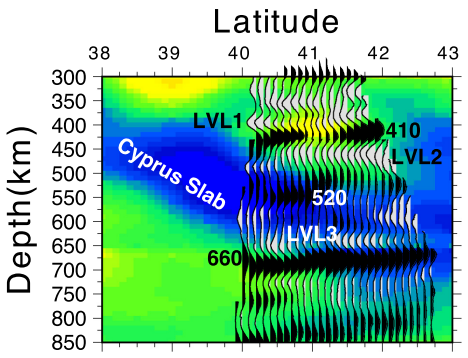

Figure 3. Common conversion point depth migrated receiver functions of the quality-controlled data set projected onto a single N–S profile using the 1-D ak135 velocity model. Background shows *P*-wave velocity variation of tomography model EU60 (Zhu *et al.* 2015). The location of the slab is indicated by high seismic velocities. The positive conversions from the 410 and 660 are observable across the profile and there is evidence for a conversion from a depth of about 520 km. The PRFs show evidence for three low-velocity layers (LVL1, LVL2, LVL3) marked by strong negative arrivals. The depth migrated section of the full data set is shown in Supporting Information Fig. S1 and shows only subtle differences. Only bins containing greater than 10 traces were included in the 2-D migration.

spatial variability that is unclear in the 1-D migration, such as the low-velocity zone associated with the 410.

We find strong correlation between the structure of the MTZ discontinuities and tomographic images that map broad-scale velocity variations associated with the subducted slab. The 410 and 660 both appear slightly deeper than average in the 3-D migrations. With our current data set, it is difficult to determine whether the depression of the 410 and 660 can be attributed solely to a reduction in *S*-wave velocity above the 410, a true depression of both discontinuities or a combination of these two. There is little evidence for significant topography of the 410 that exceeds more than a few kilometres. This is in agreement with the tomographic models of the region, which indicates that the slab impinges on the 410 to the south of our study area (Piromallo & Morelli 2003; Berk Biryol *et al.* 2011; Zhu *et al.* 2015). Therefore, it appears that the deepening of the 660 due to the presence of the subducted slab is the most likely cause of the increase in MTZ thickness to 270 km. Experimental values for the Clapeyron slope for the transition from ringwoodite to bridgmanite and magnesiowüstite vary from -1.0 MPa K^{-1} (Katsura 2003; Fei 2004) to -3.0 MPa K^{-1} (Ito & Takahashi 1989). If we attribute the observed thickening of the MTZ purely to the ringwoodite phase transition, this would indicate a temperature reduction in the range of 1000–330 K. Temperatures at the higher end of this range seem unrealistic (Peacock 1996; Stern 2002). However, recent studies suggest that a disassociation of ringwoodite into akimotoite and periclase might alter the Clapeyron slope of the 660 to values of -4 to -6 MPa K^{-1} (Yu *et al.* 2011; Hernández *et al.* 2015). This would reduce the required temperature difference between the (most likely cold) slab and ambient mantle at a depth of 660 km to explain the deepening of the 660 to a more realistic ∼160–245 K (e.g. Cottaar & Deuss 2016).

P-to-*S* conversions from the 520 are observed in the centre of the profile and seem to be colocated with the top of the subducted slab. The high amplitude of this conversion would imply a strong and sharp discontinuity. The wadsleyite–ringwoodite phase transition is thought to take place over a wide depth range of 25–60 km (Akaogi *et al.* 1989), which would not be detectable in the frequency range of our data. The depth interval for the wadsleyite to ringwoodite transition has been found to be dependent on temperature (Xu *et al.* 2008), iron and water content (Mrosko *et al.* 2015). The colocation of the subducted slab and the arrivals from about the 520 (Figs 3 and 4) makes it difficult to differentiate the source of these *P*-to-*S* conversions from a discontinuity formed due to a solid–solid phase transition or a compositional effect due to the top of the slab or the subducted oceanic Moho (Sinogeikin *et al.* 2003). The detection of an interface at this depth supports the existence of the slab in the transition zone in both scenarios, either by sharpening the phase transition through a temperature or water related effect; or by representing a direct detection of a compositional interface such as the top of the slab or the subducted Moho. The detection of a slab related interface (palaeosurface, palaeoMoho) seems to be a more suitable explanation.

Negative *P*-to-*S* converted energy that surrounds the 410 and occurs above the 660 is a prominent feature of this data set and most likely indicates the presence of low-velocity zones. Several studies have detected a low-velocity zone above the 410 (Revenaugh & Meyer 1997; Song *et al.* 2004; Tauzin *et al.* 2010) that has been interpreted as partial melting due to dehydration of hydrated material convecting upwards through the 410 (Bercovici & Karato 2003). We observe a similar low-velocity zone throughout our study region, although there is significant depth variation, most prominently a deepening from south to north. An intriguing feature of our PRFs is a negative arrival below the 410, which is interpreted as a low-velocity zone at the top of the MTZ. Hydrated wadsleyite has been found to be more buoyant than dry wadsleyite (Karato 2006), meaning hydrated material could rise to the top of the MTZ. Hydrated wadsleyite 'underplating' the 410, as suggested by Schmerr & Garnero (2007) beneath South America, is a candidate for the origin of this low-velocity zone. The 410 is observed throughout the profile even in the presence of this deeper negative arrival so the low-velocity hydrated wadsleyite does not obscure the conversion from the 410 in this location (Schmerr & Garnero 2007). The hydration of transition zone wadsleyite may occur when the slab enters the transition zone and contains hydrous mineral phases and sediments (Kuritani *et al.* 2011). The detection of the low-velocity layer beneath the 410 along the whole profile could be a remnant of this hydration process as the rollback of the Hellenic arc (currently 25–30 mm yr^{-1} towards the southwest; McClusky *et al.* 2000) would have placed the slab further to the northeast in the past, perhaps within our study region. Additionally, the 410 has a lower amplitude in the centre of the profile (Figs 3 and 4), in an area that coincides with a low-velocity zone in the tomographic model (Zhu *et al.* 2015). This low-velocity zone, along with the decreased amplitude of the 410 transition could also indicate an increased level of hydration in this area (Helffrich & Wood 1996). However, Frost & Dolejš (2007) suggest that this effect can only occur where temperatures are significantly below ambient mantle and where water contents are at or approaching saturation. The subducted slab and the long subduction history in the region might be able to provide these necessary conditions.

The PRFs migrations also show a negative conversion above the 660. Dehydration melting, due to the larger water capacity of transition zone minerals compared to the lower mantle (Hirschmann 2006; Pearson *et al.* 2014; Schmandt *et al.* 2014), would create a low-velocity zone below the 660 in regions of down-welling. In contrast, we observe low velocities above the 660. Although the phase transition in the olivine system (from ringwoodite to bridgmanite and magnesiowüstite) can explain the large scale structure of the 660, other phase transitions from garnet to calcium-rich bridgmanite have been detected in a similar pressure and temperature range

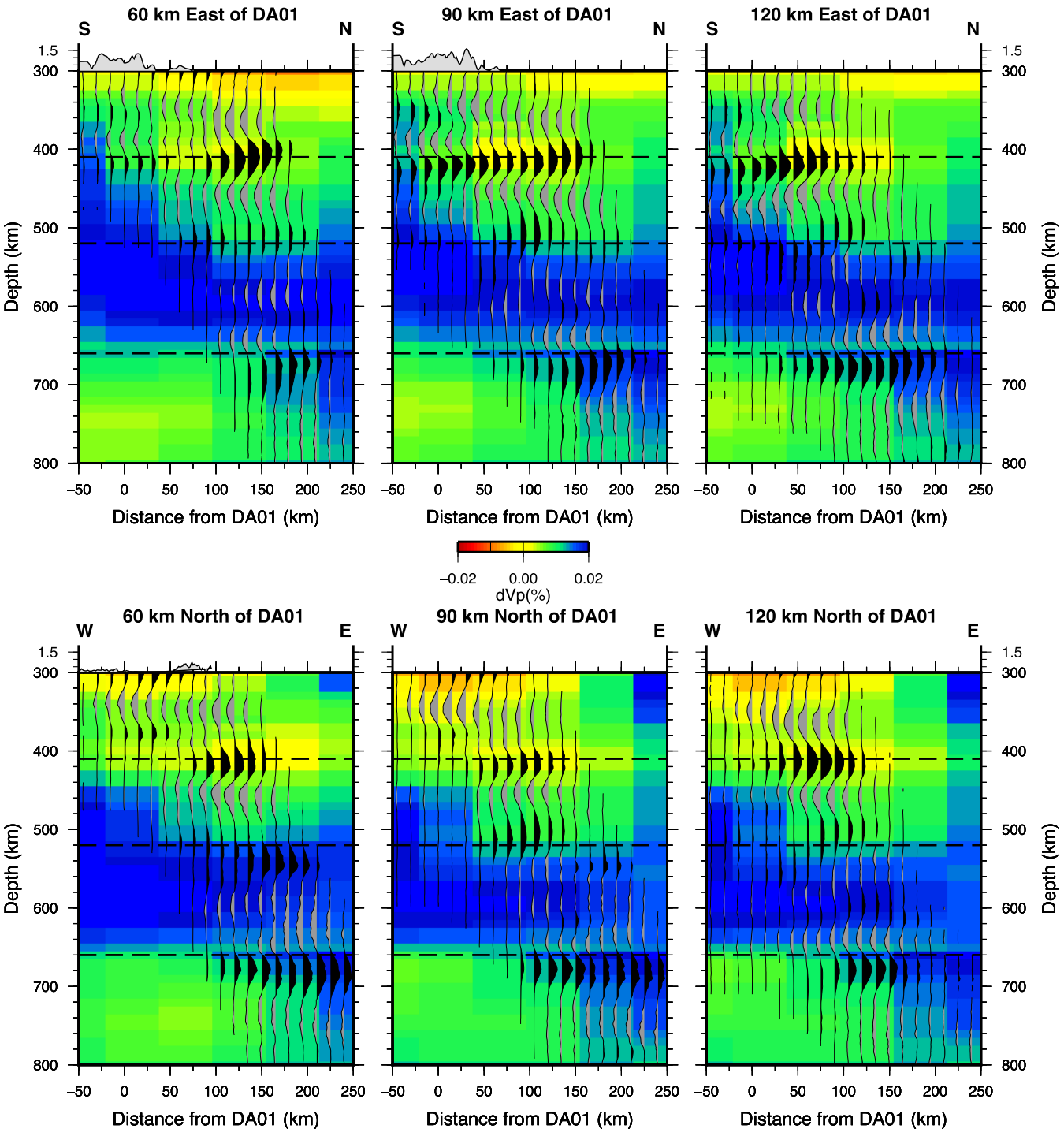

Figure 4. 3-D common conversion point migration of the 1505 highest quality receiver functions using the EU60 regional tomography model (background colour fill, Zhu *et al.* 2015). Colour scale for tomography is shown in Fig. 3. Slices through the 3-D model are shown in E–W and N–S direction (at latitudes of 40.82°, 41.09° and 41.37°; and longitudes of 30.63°, 30.90° and 31.17°). PRFs are shown as lines with positive arrivals filled in black and negative arrivals grey. Only bins containing more than five receiver functions are included, with a mean hit count of ∼15 and maximum of 89 in the centre of the study region.

(Vacher *et al.* 1998). This could lead to a more complicated structure of the 660. Such complexity has been inferred from seismic observations in other subduction zones around the planet (Simmons & Gurrola 2000; Thomas & Billen 2009). In contrast to these studies, our observations of the 660 beneath Anatolia do not show any potential splitting in the *P*-to-*S* conversions, but instead a negative velocity layer, which cannot be explained by the proposed phase transitions. Shen *et al.* (2008) and Shen & Blum (2003) attribute a low-velocity zone at these depths to the sedimentation of former subducted oceanic crust onto the 660, forming a layer dominated

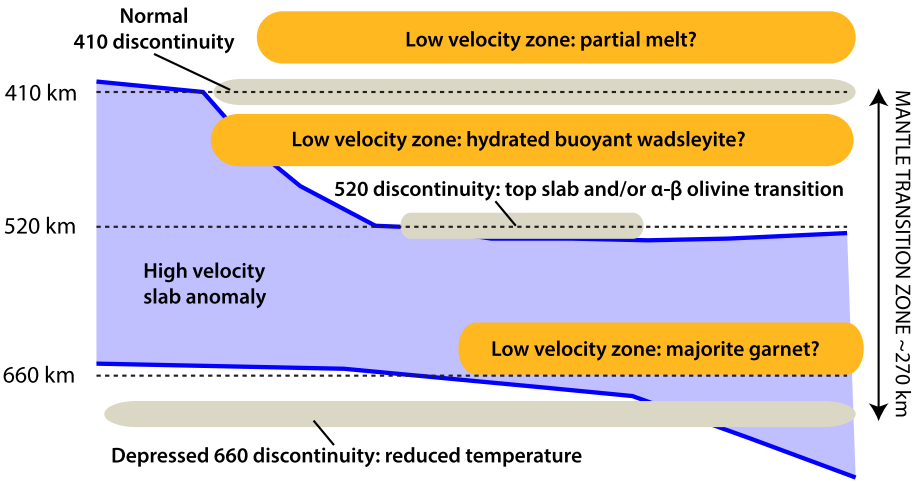

Figure 5. Interpretative sketch of the detected structure. The 410 shows little depth variation while we observe a depressed 660 due to the cooling effect of the slab. A *P*-to-*S* conversion from 520-km depth can be seen that could be the top of the slab or a sharpened wadsleyite to ringwoodite transition. The 410 is surrounded by low-velocity zones that are related to hydration from the subducting slab. The origin of the low-velocity zone above the 660 is unknown but could be related to mid-ocean ridge basalt material.

by majorite garnet. Similar proposals have been made for structures beneath western North America by Tauzin *et al.* (2013). This mechanism requires that the crustal part of the slab is stripped from the mantle component due to differential buoyancy (Karato 1997), and could explain the presence of a low-velocity anomaly above the 660. However, seismic evidence shows that some crustal material enters the lower mantle (Rost *et al.* 2008; Kaneshima 2016; Bentham *et al.* 2017). Here, we observe a low-velocity zone over the area of the profile where the slab seems to be lying flat on the 660. It remains unclear whether the slab is potentially overlying an older layer that contains crustal material, or if the velocity structure of the harzburgitic slab can be responsible for the low-velocity anomaly atop the 660.

A further explanation for low seismic velocities within the subducted slab in the lower MTZ is the presence of dense hydrous magnesium silicate phases. Low seismic velocities were observed by Brudzinski & Chen (2003) within the Tonga slab at mid to lower MTZ depths, and while this was interpreted as being associated with a metastable olivine wedge, more recent experimental work has postulated that the presence of superhydrous Phase B (ShyB) ± Phase D could also explain the results (Rosa *et al.* 2015). These phases are only stable along cold slab geotherms and have been previously linked to rapid subduction of old oceanic lithosphere along the western Pacific. The material being subducted in the Cyprus trench is believed to be comprised of ∼95Ma backarc material formed during slab rollback in the Late Cretaceous (Maffione *et al.* 2017; van der Meer *et al.* 2018). In addition to this, the age of eastern Mediterranean oceanic crust has been suggested to be as old as 340 Ma, potentially making it a remnant of the Neotethys ocean (Granot 2016). These ages would likely be sufficient to produce the thick and cold oceanic lithosphere required to stabilize ShyB within the subducted slab at MTZ depths (e.g. Litasov & Ohtani 2010), making this a viable hypothesis for the observed low-velocity layer within the Cyprus Slab.

SUMMARY AND CONCLUSIONS

This work studied a region of the upper mantle beneath northwestern Anatolia, where the Cyprus slab passes through the MTZ. The dense imaging of the transition zone with *P*-to-*S* conversions from receiver functions allows accurate observations of the interaction between the MTZ and the subducted slab. The 410 and 660 are found to be slightly deeper than the global average, though this is potentially due to low velocities in the upper mantle (Fichtner *et al.* 2013a; Zhu *et al.* 2015). The cold thermal anomaly of the subducted slab appears to deepen the 660, resulting in an MTZ thickness of approximately 270 km. We estimate that this depression of the 660 translates to a negative temperature anomaly of 160–240 K at 660-km depth compared to ambient mantle. The 410 shows little topography and we thus conclude that the slab likely passes through the 410 to the south of our study area. The 410 is bounded by strong negative arrivals above and below the main conversion. A low-velocity zone above the 410 might be related to melting of hydrated wadsleyite flowing from the transition zone and transitioning to dry olivine (Bercovici & Karato 2003), while the low-velocity zone below the 410 can be explained by buoyant hydrous wadsleyite rising to the top of the transition zone (Karato 2006; Schmerr & Garnero 2007). A conversion observed at the 520 could be due to either a sharpening of the wadsleyite–ringwoodite phase transition due to the presence of the cold slab (Xu *et al.* 2008), the presence of water extracted from the slab (Kuritani *et al.* 2011), or simply a compositional signature from the subducted Moho or the top of the crust. A low-velocity zone directly above the 660 might be related to mid-ocean ridge basalt that has been removed from the top of subducted slabs in the transition zone (Thomas & Billen 2009), or could indicate the presence of dense hydrous phases within the subducted slab (e.g. ShyB ± Phase D). The dense nature of this *P*-receiver function study allows the detection and characterization of a wide variety of features in the MTZ beneath Anatolia. The results suggest a

complex suite of processes, involving both thermal and chemical variations, occurs within and around the MTZ during the transit of a subducted slab into the lower mantle.

ACKNOWLEDGEMENTS

This work has been supported by the UK Natural Environment Research Council under grant NE/I028017/1. Seismic equipment was provided by the NERC Geophysical Equipment Facility (SEIS-UK) under loan 947. Additional funds were provided by the Bogazici University Scientific Research Projects (BAP) under grant 6922 and the Turkish State Planning Organization (DTP) under the TAM project number 2007K120610. GT was supported by the Leeds-York Doctoral Training Partnership (SPHERES) of the Natural Environment Research Council (NERC), UK (grant NE/L002574/1).

REFERENCES

Akaogi, M., Ito, E. & Navrotsky, A., 1989. Olivine-modified spinel-spinel transitions in the system Mg_2SiO_4-Fe_2SiO_4: calorimetric measurements, thermochemical calculation, and geophysical application, *J. geophys. Res.,* **94,** 15 671–15 685.

Ammon, C.J., 1991. The isolation of receiver effects from teleseismic *P*-waveforms, *Bull. seism. Soc. Am.,* **81,** 2504–2519.

Bentham, H.L.M., Rost, S. & Thorne, M.S., 2017. Fine-scale structure of the mid-mantle characterised by global stacks of PP precursors, *Earth planet. Sci. Lett.,* **472,** 164–173.

Bercovici, D. & Karato, S., 2003. Whole-mantle convection and the transition-zone water filter, *Nature,* **425,** 39–44.

Berk Biryol, C., Beck, S.L., Zandt, G. & Özacar, A.A., 2011. Segmented African lithosphere beneath the Anatolian region inferred from teleseismic *P*-wave tomography, *Geophys. J. Int.,* **184,** 1037–1057.

Bijwaard, H., Spakman, W. & Engdahl, E.R., 1998. Closing the gap between regional and global travel time tomography, *J. geophys. Res.,* **103,** 30 055–30 078.

Bock, G., 1994. Synthetic seismogram images of upper mantle structure: no evidence for a 520-km discontinuity, *J. geophys. Res.,* **99,** 15 843–15 851.

Bolfan-Casanova, N., McCammon, C.A. & Mackwell, S.J., 2006. Water in transition zone and lower mantle minerals, in *Earth's Deep Water Cycle,* pp. 57–68, eds Jacobsen, S.D. & van der Lee, S., American Geophysical Union.

Brudzinski, M.R. & Chen, W.-P., 2003. A petrologic anomaly accompanying outboard earthquakes beneath Fiji-Tonga: corresponding evidence from broadband *P* and *S* waveforms, *J. geophys. Res.,* **108,** doi:10.1029/2002JB002012.

Cavazza, W., Roure, F., Spakman, W., Stampfli, G.M. & Ziegler, P.A., 2004. *The Transmed Atlas. The Mediterranean Region from Crust to Mantle,* Springer.

Cornwell, D.G., Hetényi, G. & Blanchard, T.D., 2011. Mantle transition zone variations beneath the Ethiopian Rift and Afar: chemical heterogeneity within a hot mantle? *Geophys. Res. Lett.,* **38,** 1–6.

Cottaar, S. & Deuss, A., 2016. Large-scale mantle discontinuity topography beneath Europe: signature of akimotoite in subducting slabs, *J. geophys. Res.,* **121,** 279–292.

DANA, 2012. Dense Array for North Anatolia (DANA), Online data, International Federation of Digital Seismograph Networks, doi:10.7914/SN/YH_2012.

Dasgupta, R. & Hirschmann, M.M., 2010. The deep carbon cycle and melting in Earth's interior, *Earth planet. Sci. Lett.,* **298,** 1–13.

Faccenna, C., Bellier, O. & Martinod, J., 2006. Slab detachment beneath eastern Anatolia: a possible cause for the formation of the North Anatolian Fault, *Earth planet. Sci. Lett.,* **242,** 1–2.

Farr, T.G. *et al.*, 2007. The shuttle radar topography mission, *Rev. Geophys.,* **45,** doi:10.1029/2005RG000183.

Fei, Y., 2004. Experimentally determined postspinel transformation boundary in Mg_2SiO_4 using MgO as an internal pressure standard and its geophysical implications, *J. geophys. Res.,* **109,** 1–8.

Fichtner, A., Saygin, E., Taymaz, T., Cupillard, P., Capdeville, Y. & Trampert, J., 2013a. The deep structure of the North Anatolian Fault Zone, *Earth planet. Sci. Lett.,* **373,** 109–117.

Fichtner, A., Trampert, J., Cupillard, P., Saygin, E., Taymaz, T., Capdeville, Y. & Villasenor, A., 2013b. Multiscale full waveform inversion, *Geophys. J. Int.,* **194,** 534–556.

Flanagan, M.P. & Shearer, P.M., 1998. Global mapping of topography on transition zone velocity discontinuities by stacking *SS* precursors, *J. geophys. Res.,* **103,** 2673–2692.

Frost, D.J., 2008. The upper mantle and transition zone, *Elements,* **4,** 171–176.

Frost, D.J. & Dolejš, D., 2007. Experimental determination of the effect of H_2O on the 410-km seismic discontinuity, *Earth planet. Sci. Lett.,* **256,** 182–195.

Gilbert, H.J., Sheehan, A.F., Wiens, D.A., Dueker, K.G., Dorman, L.M., Hildebrand, J. & Webb, S., 2001. Upper mantle discontinuity structure in the region of the Tonga subduction zone, *Geophys. Res. Lett.,* **28,** 1855–1858.

Goes, S., Spakman, W. & Bijwaard, H., 1999. A lower mantle source for central European volcanism, *Science,* **286,** 1928–1931.

Granot, R., 2016. Palaeozoic-aged oceanic crust preserved beneath the eastern Mediterranean, *Nat. Geosci.,* **9,** 701–705.

Gu, Y., Dziewonski, A.M. & Agee, C.B., 1998. Global de-correlation of the topography of transition zone discontinuities, *Earth planet. Sci. Lett.,* **157,** 57–67.

Gu, Y.J. & Dziewonski, A.M., 2002. Global variability of transition zone thickness, *J. geophys. Res.,* **107,** ESE 2–1-ESE 2-17.

Hafkenscheid, E., Wortel, M.J.R. & Spakman, W., 2006. Subduction history of the Tethyan region derived from seismic tomography and tectonic reconstructions, *J. geophys. Res.,* **111,** 1–26.

Helffrich, G., 2000. Topography of the transition zone seismic discontinuities, *Rev. Geophys.,* **38,** 141–158.

Helffrich, G.R. & Wood, B.J., 1996. 410 km discontinuity sharpness and the form of the olivine α–β phase diagram: resolution of apparent seismic contradictions, *Geophys. J. Int.,* **126,** F7–F12.

Hernández, E.R., Brodholt, J. & Alfè, D., 2015. Structural, vibrational and thermodynamic properties of Mg_2SiO_4 and $MgSiO_3$ minerals from first-principles simulations, *Phys. Earth planet. Inter.,* **240,** 1–24.

Hetényi, G., Stuart, G.W., Houseman, G.A., Horváth, F., Hegedűs, E. & Brückl, E., 2009. Anomalously deep mantle transition zone below central Europe: evidence of lithospheric instability, *Geophys. Res. Lett.,* **36,** 1–6.

Hirschmann, M., 2006. Water, melting, and the deep Earth H_2O cycle, *Annu. Rev. Earth Planet. Sci.,* **34,** 629–653.

Inoue, T., Weidner, D.J., Northrup, P.A. & Parise, J.B., 1998. Elastic properties of hydrous ringwoodite (γ-phase) in Mg_2SiO_4, *Earth planet. Sci. Lett.,* **160,** 107–113.

Ito, E. & Takahashi, E., 1989. Postspinel transformations in the system Mg_2SiO_4-Fe_2SiO_4 and some geophysical implications, *J. geophys. Res.,* **94,** 10 637–10 646.

Jolivet, L., Faccenna, C. & Piromallo, C., 2009. From mantle to crust: stretching the Mediterranean, *Earth planet. Sci. Lett.,* **285,** 198–209.

Jolivet, L. *et al.*, 2013. Aegean tectonics: strain localisation, slab tearing and trench retreat, *Tectonophysics,* **597–598,** 1–33.

Kaneshima, S., 2016. Seismic scatterers in the mid-lower mantle, *Phys. Earth planet. Inter.,* **257,** 105–114.

Karato, S., 1997. On the separation of crustal component from subducted oceanic lithosphere near the 660 km discontinuity, *Phys. Earth planet. Inter.,* **99,** 103–111.

Karato, S., 2006. Remote sensing of hydrogen in Earth's Mantle, *Rev. Mineral. Geochem.,* **62,** 343–375.

Katsura, T., 2003. Post-spinel transition in Mg_2SiO_4 determined by high *P–T* in situ X-ray diffractometry, *Phys. Earth planet. Inter.,* **136,** 11–24.

Kennett, B., Engdahl, E. & Buland, R., 1995. Constraints on seismic velocities in the Earth from travel-times, *Geophys. J. Int.,* **122,** 108–124.

Kuritani, T., Ohtani, E. & Kimura, J.-I., 2011. Intensive hydration of the mantle transition zone beneath China caused by ancient slab stagnation, *Nat. Geosci.,* **4,** 713–716.

Langston, C.A., 1979. Structure under Mount Rainier, Washington, inferred from teleseismic body waves, *J. geophys. Res.,* **84,** 4749–4762.

Ligorría, J.P. & Ammon, C.J., 1999. Iterative deconvolution and receiver function estimation, *Bull. seism. Soc. Am.,* **89,** 1395–1400.

Litasov, K. & Ohtani, E., 2010. The solidus of carbonated eclogite in the system $CaO–Al_2O_3–MgO–SiO_2–Na_2O–CO_2$ to 32 GPa and carbonatite liquid in the deep mantle, *Earth planet. Sci. Lett.,* **295,** 115–126.

Maffione, M., van Hinsbergen, D.J.J., de Gelder, G.I.N.O., van der Goes, F.C. & Morris, A., 2017. Kinematics of Late Cretaceous subduction initiation in the Neo-Tethys ocean reconstructed from ophiolites of Turkey, Cyprus, and Syria, *J. geophys. Res.,* **122,** 3953–3976.

McClusky, S. *et al.*, 2000. Global positioning system constraints on plate kinematics and dynamics in the eastern Mediterranean and Caucasus, *J. geophys. Res.,* **105,** 5695–5719.

Mrosko, M., Koch-Müller, M., McCammon, C., Rhede, D., Smyth, J.R. & Wirth, R., 2015. Water, iron, redox environment: effects on the wadsleyite–ringwoodite phase transition, *Contrib. Mineral. Petrol.,* **170,** doi:10.1007/s00410-015-1163-2.

Ohtani, E., 2005. Water in the mantle, *Elements,* **1,** 25–30.

Paul, A., Karabulut, H., Mutlu, A.K. & Salaün, G., 2014. A comprehensive and densely sampled map of shear-wave azimuthal anisotropy in the Aegean–Anatolia region, *Earth planet. Sci. Lett.,* **389,** 14–22.

Peacock, S.M., 1996. Thermal and petrologic structure of Subduction zones, in *Subduction Top to Bottom,* pp. 119–133, eds Bebout, G.E., Scholl, D.W., Kirby, S.H. & Platt, J.P., American Geophysical Union.

Pearson, D.G. *et al.*, 2014. Hydrous mantle transition zone indicated by ringwoodite included within diamond, *Nature,* **507,** 221–224.

Pichon, X.L. & Angelier, J., 1979. The hellenic arc and trench system: a key to the neotectonic evolution of the eastern mediterranean area, *Tectonophysics,* **60,** 1–42.

Pichon, X.L., Angelier, J., Osmaston, M.F. & Stegena, L., 1981. The Aegean sea [and discussion], *Phil. Trans. R. Soc. Lond., A,* **300,** 357–372.

Piromallo, C. & Morelli, A., 2003. *P* wave tomography of the mantle under the Alpine–Mediterranean area, *J. geophys. Res.,* **108,** doi:10.1029/2002JB001757.

Revenaugh, J. & Meyer, R., 1997. Seismic evidence of partial melt within a possibly ubiquitous low-velocity layer at the base of the mantle, *Science,* **277,** 670–673.

Revenaugh, J. & Sipkin, S., 1994. Seismic evidence for silicate melt atop the 410-km mantle discontinuity, *Nature,* **369,** 474–476.

Robertson, A.H.F. & Dixon, J.E., 1984. Introduction: aspects of the geological evolution of the Eastern Mediterranean, in *The Geological Evolution of the Eastern Mediterranean,* pp. 1–74, Geological Society, London, Special Publications.

Rosa, A.D., Sanchez-Valle, C., Wang, J. & Saikia, A., 2015. Elasticity of superhydrous phase B, seismic anomalies in cold slabs and implications for deep water transport, *Phys. Earth planet. Inter.,* **243,** 30–43.

Rost, S., Garnero, E. & Williams, Q., 2008. Seismic array detection of subducted oceanic crust in the lower mantle, *J. geophys. Res.,* **113,** doi:10.1029/2007JB005263.

Saikia, A., Frost, D.J. & Rubie, D.C., 2008. Splitting of the 520-kilometer seismic discontinuity and chemical heterogeneity in the mantle, *Science,* **319,** 1515–1518.

Salaün, G. *et al.*, 2012. High-resolution surface wave tomography beneath the Aegean–Anatolia region: constraints on upper-mantle structure, *Geophys. J. Int.,* **190,** 406–420.

Schmandt, B., Jacobsen, S.D., Becker, T.W., Liu, Z. & Dueker, K.G., 2014. Dehydration melting at the top of the lower mantle, *Science,* **344,** 1265–1268.

Schmerr, N. & Garnero, E., 2006. Investigation of upper mantle discontinuity structure beneath the central Pacific using SS precursors, *J. geophys. Res.,* **111,** doi:10.1029/2005JB004197.

Schmerr, N. & Garnero, E.J., 2007. Upper mantle discontinuity topography from thermal and chemical heterogeneity, *Science,* **318,** 623–626.

Shearer, P. & Masters, T., 1992. Global mapping of topography on the 660-km discontinuity, *Nature,* **355,** 791–796.

Shearer, P.M., 1990. Seismic imaging of the upper mantle structure with new evidence for a 520-km discontinuity, *Nature,* **344,** 121–126.

Sheehan, A.F., Shearer, P.M., Gilbert, H.J. & Dueker, K.G., 2000. Seismic migration processing of *P-SV* converted phases for mantle discontinuity structure beneath the Snake River Plain, western United States, *J. geophys. Res.,* **105,** 19 055–19 065.

Shen, X., Zhou, H. & Kawakatsu, H., 2008. Mapping the upper mantle discontinuities beneath China with teleseismic receiver functions, *Earth Planets Space,* **60,** 713–719.

Shen, Y. & Blum, J., 2003. Seismic evidence for accumulated oceanic crust above the 660-km discontinuity beneath southern Africa, *Geophys. Res. Lett.,* **30,** doi:10.1029/2003GL017991.

Simmons, N.A. & Gurrola, H., 2000. Multiple seismic discontinuities near the base of the transition zone in the Earth's mantle, *Nat. Lett.,* **405,** 559–562.

Sinogeikin, S., 2003. Single-crystal elasticity of ringwoodite to high pressures and high temperatures: implications for 520 km seismic discontinuity, *Phys. Earth planet. Inter.,* **136,** 41–66.

Sinogeikin, S.V., Bass, J.D. & Katsura, T., 2003. Single-crystal elasticity of ringwoodite to high pressures and high temperatures: implications for 520 km seismic discontinuity, *Phys. Earth planet. Inter.,* **136,** 41–66.

Smyth, J.R. & Frost, D.J., 2002. The effect of water on the 410-km discontinuity: an experimental study, *Geophys. Res. Lett.,* **29,** 1–4.

Song, T., Helmberger, D. & Grand, S., 2004. Low-velocity zone atop the 410-km seismic discontinuity in the northwestern United States, *Nature,* **427,** 530–533.

Stampfli, G.M., 2000. Tethyan oceans, in *Tectonics and Magmatism in Turkey and the Surrounding Area,* pp. 1–23, eds Bozkurt, E., Winchester, J.A. & Piper, J.D.A., Geological Society, London, Special Publications.

Stern, R.J., 2002. Subduction zones, *Rev. Geophys.,* **40,** 3–1-3-38.

Stoffa, P.L., Buhl, P., Diebold, J.B. & Wenzel, F., 1981. Direct mapping of seismic data to the domain of intercept time and ray parameter—a plane-wave decomposition, *Geophysics,* **46,** 255–267.

Tauzin, B., Debayle, E. & Wittlinger, G., 2010. Seismic evidence for a global low-velocity layer within the Earth's upper mantle, *Nat. Geosci.,* **3,** 718–721.

Tauzin, B., van der Hilst, R.D., Wittlinger, G. & Ricard, Y., 2013. Multiple transition zone seismic discontinuities and low velocity layers below western United States, *J. geophys. Res.,* **118,** 2307–2322.

Thomas, C. & Billen, M., 2009. Upper mantle structure along a profile in the southwest Pacific, *Geophys. J. Int.,* **176,** 113–125.

Thompson, D.A., Helffrich, G., Bastow, I.D., Kendall, J.-M., Wookey, J., Eaton, D.W. & Snyder, D.B., 2011. Implications of a simple mantle transition zone beneath cratonic North America, *Earth planet. Sci. Lett.,* **312,** 28–36.

Vacher, P., Mocquet, A. & Sotin, C., 1998. Computation of seismic profiles from mineral physics: the importance of the non-olivine components for explaining the 660 km depth discontinuity, *Phys. Earth planet. Inter.,* **106,** 275–298.

van der Meer, D.G., Spakman, W., van Hinsbergen, D.J.J., Amaru, M.L. & Torsvik, T.H., 2009. Towards absolute plate motions constrained by lower-mantle slab remnants, *Nat. Geosci.,* **3,** 36–40.

van der Meer, D.G., van Hinsbergen, D.J.J. & Spakman, W., 2018. Atlas of the underworld: slab remnants in the mantle, their sinking history, and a new outlook on lower mantle viscosity, *Tectonophysics,* **723,** 309–448.

Van der Voo, R., Spakman, W. & Bijwaard, H., 1999. Tethyan subducted slabs under India, *Earth planet. Sci. Lett.,* **171,** 7–20.

Xu, W., Lithgowbertelloni, C., Stixrude, L. & Ritsema, J., 2008. The effect of bulk composition and temperature on mantle seismic structure, *Earth planet. Sci. Lett.,* **275,** 70–79.

Yu, Y.G., Wentzcovitch, R.M., Vinograd, V.L. & Angel, R.J., 2011. Thermodynamic properties of $MgSiO_3$ majorite and phase transitions near 660 km depth in $MgSiO_3$ and Mg_2SiO_4: a first principles study, *J. geophys. Res.,* **116,** doi:10.1029/2010JB007912.

Zhu, H., Bozdăg, E. & Tromp, J., 2015. Seismic structure of the European upper mantle based on adjoint tomography, *Geophys. J. Int.,* **201,** 18–52.

SUPPORTING INFORMATION

Supplementary data are available at *GJI* online.

Figure S1. CCP depth migrated receiver functions of the full data set projected onto a single N–S profile using the 1-D ak135 velocity model. Background shows *P*-wave velocity variation of tomography model EU60 (Zhu *et al.* 2015) with the colour scale shown in Fig. 3. The location of the slab is indicated by high seismic velocities. The positive conversions from the 410 and 660 are observable across the profile and there is evidence for a conversion from the 520. The PRFs show evidence for three low-velocity layers (LVL1, LVL2, LVL3) marked by strong negative arrivals.

Figure S2. (a) Radial and (b) tangential CCP migrated receiver function profiles using the ak135 1-D velocity model without (top) and with (bottom) tomographic velocity profile (Zhu *et al.* 2015). Shown is the migration of the quality-controlled data set of PRFs.

Figure S3. (a) Radial and (b) tangential CCP migrated receiver function profiles using the ak135 1-D velocity model without (top) and with (bottom) tomographic velocity profile (Zhu *et al.* 2015). Shown is the migration of the complete data set of PRFs.

Please note: Oxford University Press is not responsible for the content or functionality of any supporting materials supplied by the authors. Any queries (other than missing material) should be directed to the corresponding author for the article.